A 2.8-Angstrom-Resolution Cryo-Electron Microscopy Structure of Human Parechovirus 3 in Complex with Fab from a Neutralizing Antibody

Domanska, Ausra

2019-02

acceptedVersion

1 **2.8 Å resolution cryo-EM structure of human parechovirus 3 in**

2 **complex with Fab from a neutralizing antibody**

3 Aušra Domanska[a,b#], Justin W. Flatt[a,b], Joonas J.J. Jukonen[a,b], James A. Geraets[a,b], Sarah J.

4 Butcher[a,b#]

5

6 [a] Faculty of Biological and Environmental Sciences, Molecular and Integrative Bioscience Research

7 Programme, University of Helsinki, Helsinki, Finland

8 [b] Helsinki Institute of Life Sciences, Institute of Biotechnology, University of Helsinki, Helsinki,

9 Finland

10

11 Running title: Human parechovirus 3 in complex with Fabs

12

13 [#] Correspondence to Aušra Domanska ausra.domanska@helsinki.fi, and Sarah J. Butcher

14 sarah.butcher@helsinki.fi

15

16 Abstract includes 133 words

17 Importance includes 104 words

18 Text (without title page, abstract, importance, references, table, and figure legends) includes 4361

19 words

20 **Abstract**

21 Human parechovirus 3 (HPeV3) infection is associated with sepsis in neonates characterized by

22 significant immune activation and subsequent tissue damage. Strategies to limit infection have been

23 unsuccessful due to inadequate molecular diagnostic tools for early detection and lack of a vaccine

24 or specific antiviral therapy. Towards the latter, we present a 2.8 Å-resolution structure of HPeV3 in

25 complex with fragments from a neutralizing human monoclonal antibody AT12-015 using cryo-EM

26 and image reconstruction. Modeling revealed that the epitope extends across neighboring

27 asymmetric units with contributions from capsid proteins VP0, VP1, and VP3. Antibody decoration

28 was found to block binding of HPeV3 to cultured cells. Additionally at high-resolution, it was

29 possible to model a stretch of RNA inside the virion and from this identify the key features that

30 drive and stabilize protein-RNA association during assembly.

31 **Importance**

32 HPeV3 is receiving increasing attention as a prevalent cause of sepsis-like symptoms in neonates,

33 which despite the severity of disease, there are no effective treatments available. Structural and

34 molecular insights into virus neutralization are urgently needed, especially as clinical cases are on

35 the rise. Towards this goal, we present the first structure of HPeV3 in complex with fragments from

36 a neutralizing monoclonal antibody. At high-resolution it was possible to precisely define the

37 epitope that when targeted, prevents virions from binding to cells. Such an atomic-level description

38 is useful for understanding host-pathogen interaction, viral pathogenesis mechanisms, and for

39 finding potential cures for infection and disease.

40 **Keywords**

41 **human parechovirus 3, neutralizing antibody, genome packaging, cryo-EM**

42 **Introduction**

43 HPeV3 is a small, non-enveloped, single-stranded, positive-sense RNA virus, belonging to the

44 *Parechovirus* genus of *Picornaviridae*, which currently includes 19 genotypes most commonly

45 associated with mild gastrointestinal and respiratory illness (1, 2). Increased availability of sequence

46 data in clinical settings has clarified that HPeV3 causes the most virulent infections of the HPeVs,

47 particularly in infants less than 3 months of age where sickness can trigger a sepsis-like

48 dysregulated host response often involving the central nervous system (3-9). In cases of acute

49 meningitis or encephalitis where patients may develop abnormal white matter lesions, neurological

50 sequelae and even death may occur (10-15). To date, no effective treatments for HPeV3 infection

51 are available, highlighting the urgent need for a greater understanding of the structural and

52 molecular basis for HPeV3 neutralization, especially as epidemics are likely to continue (2, 16-18).

53 The HPeV3 virion is composed of 60 copies of the three structural proteins (VP0, VP1, and VP3)

54 that fit together to form a 28-nm-diameter icosahedral shell around the ~7.3 kb single-stranded

55 RNA viral genome (19). The genome encodes a single polyprotein that during infection is

56 subsequently cleaved into all the essential capsid components and replication proteins (2A, 2B, 2C,

57 3A, 3B, 3C and 3D) (20). Exactly how the HPeV3 particle gets assembled is poorly understood and

58 research is ongoing.

59 In the case of HPeV1, recent work has shown that newly synthesized viral RNA contains ~60

60 spatially defined, conserved sequence/structure GXUXUXXU motifs that bind capsid proteins,

61 driving genome encapsidation and efficient capsid self-assembly (21, 22). Assembled capsids lack

62 cleavage of VP0 into VP2 and VP4 products, resulting in a shell made of three proteins rather than

63 the four found in most other picornaviruses. These three proteins that constitute the asymmetric unit

64 get incorporated into pentameric modules, 12 of which form the complete icosahedral capsid of the

65 virus.

66 Around each of the pentamers there is a depression referred to as the canyon. The tips of the three-

67 fold symmetric propeller-like protrusions are adjacent to this canyon.

68 The VP1 C terminus of several human parechoviruses (e.g., HPeV -1, -2, -4, and -5) contains an

69 arginine-glycine-aspartic acid (RGD) motif that can attach to αVβ1, αVβ3, and αVβ6 integrin

70 receptors (23, 24). HPeV3 lacks the RGD motif and thus likely uses a different, as yet unknown,

71 receptor for cell entry (25). Reliance on a different receptor may alter tissue tropism and could

3

72   explain why HPeV3 infections have different clinical and epidemiological features compared to

73   other HPeV genotypes.

74   Human monoclonal antibodies (mAbs) can be exploited to gain valuable insights into the structural

75   basis for neutralizing activity, which in turn can be used for developing effective treatments. High-

76   resolution mapping of mAb binding sites at the HPeV3 capsid surface allows for identification of

77   epitopes recognized by the humoral immune system and may begin to provide mechanistic clues

78   into immune surveillance, evasion, or escape. Here, using high-resolution cryo-EM we define such

79   an epitope, that when targeted by a human monoclonal antibody, blocks attachment of virions to

80   host cells; hence also describing a potential site for receptor binding.

81   **Results**

82   **Cryo-EM structure of the HPeV3-Fab AT12-015 complex**

83   Cryo-grids containing vitrified Fab-labeled virus were imaged and after data processing in

84   RELION , a total of 74,927 particle projections were selected, which yielded a 3D reconstruction

85   extending to 2.8 Å resolution according to the gold-standard Fourier shell correlation 0.143

86   criterion (Table 1 and Figure 1A) (26). Fab decoration on the capsid surface helped to assign

87   particle orientations during data processing. The capsid was resolved to 2.3 Å, whereas small

88   stretches of capsid associated RNA and peripheral regions of Fab were defined at a resolution lower

89   than 3.5 Å (Figure 1B). In the structure, Fab molecules bind to symmetry-related sites at the tips of

90   the propellers on the surface of the virion (Figure 2A-C). For fitting, large regions of the map

91   showed clear delineation of secondary structural elements, including amino acid and nucleic acid

92   densities (Figure 2D-G). In this manner, we could accurately map the antibody footprint on the

93   capsid surface, as well as visualize an RNA base-stacking motif that stably anchors the genome to

94   the capsid via interaction with a tryptophan residue (Trp 24) in the HPeV3 VP3 coat protein (Figure

95   2F and G).

96   **Characterization of the Fab AT12-015 Epitope**

4

97   In the reconstruction, the signal related to the Fab heavy and light chains is roughly as strong as that

98   of the viral capsid, indicating 100% occupancy of the 60 available binding sites on the virion

99   (Figure 1B). The quality of the map was such that we could fit atomic coordinates for the Fab, as

100   well as for the three viral coat proteins, and this was followed by MDFF all-atom refinement.

101   Results from flexible fitting revealed that the Fab targets an extended, solvent-accessible VP0-VP1-

102   VP1′-VP3′ (′ denotes a neighboring asymmetric unit) conformational epitope. There is no evidence

103   of induced structural changes in any of the capsid proteins upon Fab binding based on a comparison

104   to the crystal structure of HPeV1 (rmsd 0.6) (21). Using a 3.6 Å distance cutoff we identified 28

105   capsid residues forming the epitope and 29 Fab residues that form the paratope (Figure 3A).

106   Residues from the capsid that are involved in forming the immune complex are conserved among

107   HPeV3 strains, but not for HPeV1 or other parechovirus types. Six hydrogen bonds at the interface

108   were identified, three from the heavy chain: Arg 58 to VP1 residue Asp 87, Tyr 59 to VP1 residue

109   Asn 138, and Arg 99 to VP3 residue Leu 252, and three from the light chain: Ser 28 to VP0 residue

110   Glu 285, Asn 93 to VP1 residue Asp 137, and Ser 30 to VP3 residue Gly 207, that have angles in

111   the range of 138-180º and are closely spaced to stably interact with exposed backbone nitrogen and

112   oxygen atoms in the capsid proteins (Figure 3B). An additional hydrogen bond may form between

113   the Fab light chain residue Ser 67 and VP3 residue Gln 209. However, the density in this area of the

114   map was weak and because of this it was not possible to assess whether suitable geometric

115   conditions were met for the interaction to occur other than the fact that the residue pair was in close

116   proximity. One salt bridge between heavy chain amino acid Glu 105 and VP3 residue His 206 was

117   inferred by the fact that centroids of the oppositely charged functional groups of the residues were

118   within a 4 Å cutoff; and the Glu carbonyl oxygen atom was within 4 Å distance from the nitrogen

119   atom of the His side chain (Figure 3B). This His 206 is centrally located in the footprint for the

120   antibody and it was recently reported to be critical for binding and neutralization based on

121   experimental selection of an antibody AT12-015 resistant HPeV3 variant (VP3 His 206 to Tyr) (27).

122

Human monoclonal antibody AT12-015 prevents HPeV3 entry into cells

To probe HPeV3 A308/99-specific neutralization, we assayed whether binding of virions to human intestinal HT29 cells was blocked by the presence of human monoclonal antibody AT12-015 (Figure 4). For antibody-mediated blocking, we pre-incubated equivalent amounts of virus with antibody at 30, 3, 0.3, 0.03, 0.003 µg/ml final concentrations for 1 hour at 37° C and then added the complexes to cells. Cellular attachment proceeded under ice-cold conditions for 1 hour and afterwards unbound virions were removed with a series of gentle PBS wash steps. Cold binding ensures that HPeV3 remains at the surface of cells and is not internalized. When preformed antibody-decorated virions were added, either from mixing HPeV3 with stock or 1:10 dilution of antibody, which is equivalent to 30 and 3 µg/ml of antibody respectively, no fluorescence signal was observed on the surface of HT29 cells similar to the mock infection (no virus) and antibody controls (Figure 4A – 30 µg/ml, 3 µg/ml, mock, AT12-015 no virus). Small-sized clusters of virions were observed at excess levels of antibody (Figure 4A - 30 µg/ml, and 3 µg/ml). In contrast, staining was clearly visible on the surface of cells incubated with HPeV3 alone, as well as with higher dilutions of antibody, and fluorescence intensity was weaker at 1:100 dilution (0.3 µg/ml) albeit with a high standard deviation (Figure 4A and B – 0.003 µg/ml, 0.03 µg/ml, and 0.3µg/ml). Virus mixed with 1:100 of antibody showed neutralizing activity without any apparent clumping (Figure 4B – 0.3 µg/ml). In addition, to be sure that the observed block in virus binding was due to AT12-015 and not because of premixing, we included an unrelated antibody as a control (Figure 4C). This control antibody AM28 recognizes a conformational epitope in HPeV1 but does not bind to the capsid of HPeV3 (41). Taken together, these results indicate that AT12-015 neutralizes HPeV3 A308/99 infection at least in part extracellularly, but this does not rule out additional downstream (post attachment) inhibitory effects.

RNA inside the HPeV3 capsid

148   The HPeV3 virion contains ~7.3 kb of mostly unstructured single-stranded RNA genome. In the

149   assembled particle, roughly 25% of the RNA adopts a defined conformation near the inner capsid

150   surface, lining symmetry-related sites directly beneath the icosahedral five-fold vertices (19). For

151   parechoviruses, detailed structural analysis of genome-capsid interactions has only been carried out

152   for HPeV1 (21). Here we performed a similar analysis for HPeV3. The inside of our 2.8 Å HPeV3

153   map shows stretches of RNA in the same region as defined for HPeV1. The RNA has a defined

154   tertiary structure, forming a single-stranded loop with a significant portion involved in a rigid base-

155   stacking motif that is capped by an aromatic side chain residue Trp 24 of VP3 with a small

156   conjugated π system (Figure 5A and B). In this way, the tryptophan has stabilized its π orbitals to a

157   resonance level with the aromatic orbitals of adjacent RNA bases to enable efficient packaging and

158   formation of stable virions (Figure 2G). EM density for the planar stacking profile is well-resolved,

159   on the order of 25 Å in length, before reaching a helix-coil transition (Figure 5B). Coordinates for

160   the six RNA nucleotides from previous structural work on the HPeV1 virion are in good agreement

161   with our modeled stacking motif. We fitted eight bases of RNA beneath the capsid, which included

162   a portion of the packaging sequence described recently for HPeV1 (22). The final sequence docked

163   was U^0-G^1-G^2-U^3-A^4-U^5-U^6 U^n. Using the RNA motif we searched the HPeV3 A308/99 genome

164   (Genbank code AB084913) and identified 33 sequences that contained G^1-$purine^2$-U^3-$purine^4$-U^5,

165   13 of which include the full motif X^0-G^1-$purine^2$-U^3-$purine^4$-U^5-X^6-X^7-U^8.

166   In addition to modeling the Trp 24-RNA contact in the cryo-EM structure, two other residues from

167   the same VP3 strand, Lys 21 and Tyr 22, were found to interact with a neighboring RNA loop.

168   These residues, along with Trp 24, in the context of the assembled pentamer, appear to be key for

169   stabilizing the stacked RNA below the capsid vertex (Figure 5C). In fact, mutation of two of the

170   amino acids, either Tyr 22 or Trp 24 to alanine, in HPeV1 is lethal confirming their essential role in

171   virion stability (22). Other capsid residues that further support the RNA loop under the vertex were

172   identified in VP1, as well as VP3. Specifically, VP1 residues Arg 202, Cys203, and Asn 205, and

173   VP3 residues Ala 18, Ser 19, Thr20, Leu 44, Thr 47, Arg 58, Phe 60, Tyr 61, and Arg 71, many of

174   which are aromatic or positively charged, form important RNA base and backbone contacts, as well

175   as complement the negative charge of the RNA (Figure 5D). In HPeV1, mutations of VP1 residues

176   Arg 202 and Cys 203 to Ala as well as VP3 residues Thr 44, Arg 55, and Arg 68 to Ala (VP3

177   residues Thr47, Arg 58, and Arg 71 in our structure) were shown to be lethal, indicating that these

178   residues are important for stability, possibly at the level of RNA packaging and virion assembly

179   (22).

180

181   **Discussion**

182   Exact knowledge of the structural, antigenic, and immunogenic features of HPeV3 is essential for

183   understanding host-pathogen interaction, viral pathogenesis mechanisms, and for finding potential

184   cures for infection and disease, which is pressing as HPeV3 outbreaks are widespread and may

185   cause severe sepsis-like syndrome in neonates. Recently, we determined a structure of HPeV3 in

186   complex with Fab fragments from a human monoclonal antibody AT12-015 by cryo-EM (19).

187   However, the strain of virus used in that study, HPeV3 isolate 152037, was not neutralized by

188   addition of AT12-015. Furthermore the resolution of the reconstruction was only at 15 Å, which

189   prevented atomic characterization of the epitope on the surface of the viral capsid. Here we report a

190   2.8 Å-resolution cryo-EM structure of an AT12-015 Fab-decorated HPeV3 virion (isolate A308/99).

191   We have shown in a recent study that this particular virus isolate is neutralized by monoclonal

192   antibody AT12-015 (27). In the high-resolution structure, the antigen-antibody interface was well-

193   defined and modeling of viral coat proteins and Fab molecules into density revealed an extended

194   conformational epitope across the interface of adjacent asymmetric units, involving residues from

195   different parts of neighboring VP0, VP1, and VP3 chains spatially juxtaposed by the structure of the

196   capsid. When bound, monoclonal AT12-015 prevented virus attachment to target HT29 cells except

197   for at high dilutions of antibody, indicating that neutralization may occur extracellularly and not by

198   a post-attachment mechanism. In this way, we were able to identify the epitope of AT12-015 and

199 determine how the antibody works against HPeV3 A308/99. In addition, the 2.8 Å map provided the

200 most complete picture yet of ordered RNA on the inside of a human parechovirus.

201 Antibody AT12-015 was first isolated from the immune repertoire of a person with HPeV3 infection

202 using the AIMSelect method and it broadly recognizes strains of HPeV3 but only neutralizes the

203 prototype A308/99 virus that we used in the study (19, 27, 28). At high resolution we could clearly

204 specify the conserved conformational epitope shared among HPeV3 strains, including solvent-

205 accessible atoms in the interface region, which now includes contributions from VP0 (Glu 285, Asn

206 289), VP1 (Asn 85, Asp 87, Thr 135-Asn 138, Lys 140, Thr 141, Arg 184), VP1' (Pro 215-Ser 218),

207 and VP3' (Lys 99, Tyr 100, Val 119, Thr 121, Met 132, Thr 167, Asp 169, His 206-Gln 209, Leu

208 252, Val 253; Figure 3A). No structural changes were induced upon Fab-virion complex formation.

209 Atomic-level characterization brings clarity to exactly how Fab AT12-015 binds to the virion. Of

210 particular interest is His 206 of VP3 as it was recently shown that an HPeV3 A308/99 variant

211 mutated at this residue position to Tyr escapes neutralization by AT12-015 (27). Our results provide

212 important context to this observation by showing that the nitrogen atom of VP3 His 206 forms a salt

213 bridge with the carbonyl oxygen of Glu 105 in the Fab heavy chain at the center of the antibody

214 footprint (27). Thus we can confirm a key role for VP3 His 206 in driving Fab-virion complex

215 formation.

216 Because antibodies often prevent virus attachment and entry into target cells, we tested whether

217 AT12-015 blocks HPeV3 A308/99 binding to human intestinal HT29 cells. We found that mixing

218 antibody with virions under saturating conditions efficiently inhibits viral adhesion to cells and this

219 effect is only reversed at high dilutions of the antibody. At high antibody concentrations the

220 inhibitory effect may arise in part due to clustering of AT12-015-labeled virions, but specific

221 targeting rather than generalized immune complex formation is supported by the fact that of all

222 HPeV3 strains bound by AT12-015, only isolate A308/99 is neutralized as measured by quantitative

223 RT-PCR (27). Neutralization occurs thus presumably by either directly or indirectly preventing

224 receptor engagement. To date, little is known about HPeV3 receptor and co-receptor dependencies

9

225   as it lacks the RGD motif and hence probably utilizes an uptake mechanism that differs from other

226   parechovirus types. This could account for type-specific neutralization, and in general usage of a

227   different receptor by HPeV3 likely influences tropism and thus the unique disease severity in the

228   human population.

229   It has become increasingly appreciated in recent years that for single-stranded RNA viruses, the life

230   cycle is in part regulated by the secondary and tertiary structure of their genomes, hence the current

231   high priority to understand protein-(single-stranded) RNA recognition motifs and RNA sequence-

232   specific folding as it occurs in assembled virions (22, 29-33). Such information may help with

233   efforts to inhibit viral propagation, as well as in nanotechnology applications aimed at harnessing

234   either virus or virus-like systems for efficient gene delivery (34). Based on our cryo-EM data, we

235   propose a mechanism for adding HPeV3 RNA to assembling shells that utilizes π electron

236   delocalization from VP3 side chain Trp 24 to assist with nucleotide binding. Here, at the

237   mechanistic level, RNA folding is stabilized by a capsid-locking step where Trp 24, accessible on

238   the inner surface of capsid protein VP3, forms a geometrically favorable short-range stacking

239   interaction with a purine, which is then further strengthened by long-range interactions as a result of

240   electronic resonance through further stacking of adjacent nucleotides. The 14 additional highly

241   conserved capsid residues: VP1 Arg 202, Cys 203 and Asn 205, VP3 Ala 18, Ser 19, Thr 20, Lys 21,

242   Tyr 22, Leu 44, Thr 47, Arg 58, Phe 60, Tyr 61, and Arg 71 help to position the ordered RNA loop

243   against the inside of the capsid. From an evolutionary perspective, this means that over time the

244   inner surface of the virus has been fine-tuned to orchestrate the interaction between VP3 Trp 24 and

245   discrete sequences of genomic RNA, and that likewise the spacing of recognition motifs on the

246   HPeV3 genome has been thermodynamically optimized so as to minimize the free energy of capsid

247   assembly.

248   **Methods**

249   *Virus sample preparation*

250   Human colon adenocarcinoma (HT29) cells were propagated in McCoy's 5A medium supplemented

251   with 1X non-essential amino acids, 1X antibiotic-antimycotic, and 10% fetal bovine serum with the

252   culture condition of 37ºC and 5% CO_2. Cells were grown to ~90% confluency before inoculating

253   with human parechovirus 3 (HPeV3) isolate A308/99 at a multiplicity of infection of 0.1. HPeV3

254   A308/99 was grown in fresh medium as described above except that the medium was slightly

255   modified to contain 1 mM $MgCl_2$, 20 mM HEPES pH 7.4 and no FBS. Inoculated cells were

256   incubated at 37ºC for 3 days. Cells and medium were harvested. At this point concentration of

257   HEPES was increased to 40 mM final concentration. The cells were opened by three freeze-thaw

258   cycles and virus-containing medium was clarified by low-speed centrifugation. Afterwards the

259   supernatant was carefully removed and concentrated via ultrafiltration using Centricon units with a

260   cut-off at 100 kDa in weight. For purification, we applied a CsCl density gradient (top - 1.2502 g

261   cm^{-3}, bottom - 1.481 g cm^{-3}) combined with ultracentrifugation (32,000 rpm, 4ºC) for 18 hours in a

262   Beckman type SW41 Ti rotor. The virus band was collected and the buffer exchanged into 1X TNM

263   buffer: 10 mM Tris-HCl, pH 7.5, 150 mM NaCl, 1 mM $MgCl_2$. Ultracentrifugation and buffer

264   exchange were repeated. Concentration was estimated by Coomassie-blue-stained SDS-PAGE gel,

265   where different concentrations of bovine serum albumin solution were used as standards. Infectivity

266   was measured using a TCID50 endpoint dilution assay.

267   *Generation of antigen-binding Fab fragment*

268   HPeV3 A308/99-specific monoclonal antibody (AT12-015) was obtained from AIMM Therapeutics

269   (the Netherlands). AT12-015 antibody was digested to produce antigen-binding Fab fragments using

270   the Pierce Fab micro preparation kit (Pierce). The Fab concentration was assessed by Coomassie-

271   blue-stained SDS-PAGE gel, where different concentrations of bovine serum albumin solution were

272   used as standards. For complex formation, 30 µL of 0.1 µg/µL virus and 9 µL of 0.1 µg/µL antibody

273   were mixed (1:60 molar ratio) and incubated for 1 hour at 37ºC.

274   *Cryo-EM data acquisition*

275   Sample volumes of 3 µL of purified HPeV3 A308/99-Fab complex were applied to glow-discharged

276   ultrathin carbon-coated lacey 400-mesh copper grids (Ted Pella product #01824) and vitrified using

277   a custom-made manual plunger. Cryo-grids were visualized with a FEI Titan Krios electron

278   microscope operating at 300 kV accelerating voltage, at a nominal magnification of 75,000× using a

279   FEI Falcon II direct electron detector, corresponding to a pixel size of 1.06 Å on the specimen level.

280   In total, 6,541 images with defocus values in the range of -0.5 to -2.5 µm were recorded in movie

281   mode with 1 second of total acquisition time. Each movie contained 18 frames with an accumulated

282   dose of about 48 electrons per $Å^2$.

283   *Image processing and 3D reconstruction*

284   Dose-fractionated image stacks containing frames from 2 to 17 were subjected to beam-induced

285   motion correction using MotionCor2 (35). Estimation of contrast transfer function parameters for

286   each micrograph was done using Gctf (36). Particle selection, 2D classification, and 3D

287   classification were performed on an unbinned dataset (1.06 Å/pix, 480 pixel box size) using

288   RELION 2.0 (26). In total, 217,212 particle projections were selected. After reference-free 2D

289   classification in RELION in the best classes containing 179,457 particle projections were used for

290   further processing. A ~ 10 Å reference map generated in AUTO3DEM from a modest-sized dataset

291   of 2050 particle images collected on a FEI Tecnai TF20 cryo-electron microscope filtered to 60 Å

292   was used for initial maximum-likelihood-based 3D classification (37). Three classes accounting for

293   74,927 particles were selected for 3D refinement and reconstruction. During post-processing step in

294   RELION the map was masked with a soft mask and sharpened using a B-factor -70 $Å^2$. The final

295   refinement resulted in a 2.8 Å map based on the gold-standard Fourier shell correlation 0.143

296   criterion. Local resolution was determined using ResMap with the unsharpened map as an input

297   (38).

298   *Atomic model building and refinement*

299   An initial atomic model for the HPeV3 A308/99-Fab complex was generated using I-TASSER and

300   SWISS-MODEL based on the crystal structure of the HPeV1 virion (PDB ID: 4Z92) and Fab

301 fragments of human monoclonal antibody AM28 (PDB ID: 4UDF) (21, 39-41). Docking of atomic

302 coordinates was done manually using UCSF Chimera and the fit was further optimized using the

303 'Fit in Map' command (42). Inspection and further refinement was done using Coot 0.8.8 and this

304 served as input for molecular dynamics flexible fitting (MDFF) (43). The MDFF program was used

305 together with NAMD and VMD to further enhance the fit of models into cryo-EM density (44-46).

306 A scale factor of 1 was employed to weigh the contribution of the cryo-EM map to the overall

307 potential function used in MDFF. Simulations included 20,000 steps of minimization and 100,000

308 steps of molecular dynamics under implicit solvent conditions with secondary structure restraints in

309 place. To achieve the best fit of the model to the cryo-EM density three iterations between Coot and

310 MDFF were performed with the last step being relaxation of the structure by an energy

311 minimization step using MDFF. For hydrogen bond detection at the virus-antibody interface we

312 examined structure in UCSF Chimera using a strict distance cutoff of 3.6 Å and for geometrical

313 constrains we only included hydrogen bonds within the range of 138 - 180º (47, 48). RNA-protein

314 interface was analyzed in UCSF Chimera using the same (3.6 Å) distance cutoff.

315 *Binding assay*

316 HT29 cells were seeded on 96-well plates at a density of 40000 cells per well in the same culture

317 conditions as during virus sample preparation. Antibody AT12-015 was incubated as stock (0.5

318 mg/ml) or as a dilution (1:10, 1:100, 1:1000, 1:10000) with 1x CsCl-gradient purified HPeV3

319 giving final antibody concentrations of 30 µg/ml, 3 µg/ml, 0.3 µg/ml, 0.03 µg/ml and 0.003 µg/ml.

320 As a control, an HPeV1-specific antibody AM28 was added to virus similar as AT12-015.

321 Specifically, 2 µl of antibody was mixed with 2 µl of virus ($8 * 10^5$ pfu/ml) for 1 hour at 37 °C.

322 The incubation took place in McCoy's 5A medium supplemented with 1X GlutaMAX, 1X non-

323 essential amino acids, 1X antibiotic-antimycotic, 20 mM HEPES, and 30 mM $MgCl_2$. Plates

324 containing cells and tubes containing antibody-virus complexes were placed on ice and allowed to

325 cool. Growth medium of the cells was exchanged to cold-binding medium. Antibody-virus

326 complexes, as well as either viruses or antibodies alone were then added to cells and incubated for 1

13

327   hour at ice-cold temperature. After incubation, cells were washed 3 times with 0.5 % BSA-PBS and

328   incubated for 1 hour with primary antibody AT12-015 diluted in 0.5% BSA-PBS. After three

329   additional washing steps and fixing (4% paraformaldehyde 30mins), a secondary antibody was

330   added for 1 hour. The procedure up until staining with secondary antibody was completed on ice. A

331   further series of washes was carried out and Hoechst (1 ug/ml) was added for visualization of cell

332   nuclei. Wells were then washed a last time and plates were sealed for imaging.

333   *High content imaging and analyses*

334   All experiments were performed in 96-well plates (Perkin Elmer) and images were acquired using

335   the automated fluorescence microscope CellInsight from Thermo Scientific. Image analysis was

336   completed using CellProfiler (http://cellprofiler.org)).

337   *Accession numbers*

338   The final density map has been deposited to Electron Microscopy Databank (EMDB) with

339   accession code EMD-0069 (https://www.ebi.ac.uk/ebisearch/search.ebi?db=allebi&query=emd-

340   0069&requestFrom=searchBox). The atomic model has been deposited to Protein Databank (PDB)

341   with accession code 6GV4 (http://www.ebi.ac.uk/pdbe/entry/pdb/6gv4).

342

343   **Acknowledgements**

359   **Author Contributions**

360   Conceptualization (A.D., S.J.B.);   formal analysis (A.D.); data curation (A.D., S.J.B.);

361   investigation (A.D., J.W.F., J.J.J.J.); methodology (A.D., J.W.F., J.J.J.J., J.A.G., S.J.B.); software

362   (J.A.G.); validation (A.D., J.W.F.); visualization (A.D.); manuscript writing (J.W.F.); manuscript

363   revision (A.D., J.A.G., S.J.B.); funding acquisition (A.D., S.J.B.); supervision (A.D., S.J.B.);

364   project administration (S.J.B.).

365   **Declaration of Interests**

366   The authors declare no competing interests.

367   **References**

368   1.   **Ito M, Yamashita T, Tsuzuki H, Takeda N, Sakae K.** 2004. Isolation and identification of

369   a novel human parechovirus. J Gen Virol **85:**391-398.

370   2.   **Olijve L, Jennings L, Walls T.** 2018. Human Parechovirus: an Increasingly Recognized

371   Cause of Sepsis-Like Illness in Young Infants. Clin Microbiol Rev **31**.

372   3.   **Khatami A, McMullan BJ, Webber M, Stewart P, Francis S, Timmers KJ, Rodas E,**

373   **Druce J, Mehta B, Sloggett NA, Cumming G, Papadakis G, Kesson AM.** 2015. Sepsis-

374   like disease in infants due to human parechovirus type 3 during an outbreak in Australia.

375   Clin Infect Dis **60:**228-236.

376   4.   **Boivin G, Abed Y, Boucher FD.** 2005. Human parechovirus 3 and neonatal infections.

377   Emerg Infect Dis **11:**103-105.

378   5.   **Levorson RE, Jantausch BA, Wiedermann BL, Spiegel HM, Campos JM.** 2009. Human

379   parechovirus-3 infection: emerging pathogen in neonatal sepsis. Pediatr Infect Dis J **28:**545-

380   547.

381   6.   **Selvarangan R, Nzabi M, Selvaraju SB, Ketter P, Carpenter C, Harrison CJ.** 2011.

382   Human parechovirus 3 causing sepsis-like illness in children from midwestern United

383   States. Pediatr Infect Dis J **30:**238-242.

384   7.   **Wolthers KC, Benschop KS, Schinkel J, Molenkamp R, Bergevoet RM, Spijkerman IJ,**

385   **Kraakman HC, Pajkrt D.** 2008. Human parechoviruses as an important viral cause of

386   sepsislike illness and meningitis in young children. Clin Infect Dis **47:**358-363.

387   8.   **Sano K, Hamada H, Hirose S, Sugiura K, Harada S, Koizumi M, Hara M, Nishijima**

388   **H, Taira M, Ogura A, Ogawa T, Takanashi JI.** 2018. Prevalence and characteristics of

389   human parechovirus and enterovirus infection in febrile infants. Pediatr Int **60:**142-147.

390   9.   **Harvala H, Calvert J, Van Nguyen D, Clasper L, Gadsby N, Molyneaux P, Templeton**

391   **K, McWilliams Leitch C, Simmonds P.** 2014. Comparison of diagnostic clinical samples

392   and environmental sampling for enterovirus and parechovirus surveillance in Scotland, 2010

393   to 2012. Euro Surveill **19**.

394   10. **Britton PN, Dale RC, Nissen MD, Crawford N, Elliott E, Macartney K, Khandaker G,**

395   **Booy R, Jones CA, Investigators P-A.** 2016. Parechovirus Encephalitis and

396   Neurodevelopmental Outcomes. Pediatrics **137:**e20152848.

397   11. **Schuffenecker I, Javouhey E, Gillet Y, Kugener B, Billaud G, Floret D, Lina B, Morfin**

398   **F.** 2012. Human parechovirus infections, Lyon, France, 2008-10: evidence for severe cases.

399   J Clin Virol **54:**337-341.

400   12. **Sedmak G, Nix WA, Jentzen J, Haupt TE, Davis JP, Bhattacharyya S, Pallansch MA,**

401   **Oberste MS.** 2010. Infant deaths associated with human parechovirus infection in

402   Wisconsin. Clin Infect Dis **50:**357-361.

403   13.   **van Zwol AL, Lequin M, Aarts-Tesselaar C, van der Eijk AA, Driessen GA, de Hoog**

404   **M, Govaert P.** 2009. Fatal neonatal parechovirus encephalitis. BMJ Case Rep **2009**.

405   14.   **Verboon-Maciolek MA, Groenendaal F, Hahn CD, Hellmann J, van Loon AM, Boivin**

406   **G, de Vries LS.** 2008. Human parechovirus causes encephalitis with white matter injury in

407   neonates. Ann Neurol **64:**266-273.

408   15.   **Vergnano S, Kadambari S, Whalley K, Menson EN, Martinez-Alier N, Cooper M,**

409   **Sanchez E, Heath PT, Lyall H.** 2015. Characteristics and outcomes of human parechovirus

410   infection in infants (2008-2012). Eur J Pediatr **174:**919-924.

411   16.   **Aizawa Y, Izumita R, Saitoh A.** 2017. Human parechovirus type 3 infection: An emerging

412   infection in neonates and young infants. J Infect Chemother **23:**419-426.

413   17.   **Esposito S, Rahamat-Langendoen J, Ascolese B, Senatore L, Castellazzi L, Niesters**

414   **HG.** 2014. Pediatric parechovirus infections. J Clin Virol **60:**84-89.

415   18.   **Wildenbeest JG, Harvala H, Pajkrt D, Wolthers KC.** 2010. The need for treatment

416   against human parechoviruses: how, why and when? Expert Rev Anti Infect Ther **8:**1417-

417   1429.

418   19.   **Shakeel S, Westerhuis BM, Domanska A, Koning RI, Matadeen R, Koster AJ, Bakker**

419   **AQ, Beaumont T, Wolthers KC, Butcher SJ.** 2016. Multiple capsid-stabilizing

420   interactions revealed in a high-resolution structure of an emerging picornavirus causing

421   neonatal sepsis. Nat Commun **7:**11387.

422   20.   **Stanway G, Hyypiä T.** 1999. Parechoviruses. J Virol **73:**5249-5254.

423   21.   **Kalynych S, Palkova L, Plevka P.** 2016. The Structure of Human Parechovirus 1 Reveals

424   an Association of the RNA Genome with the Capsid. J Virol **90:**1377-1386.

425   22.   **Shakeel S, Dykeman EC, White SJ, Ora A, Cockburn JJB, Butcher SJ, Stockley PG,**

426   **Twarock R.** 2017. Genomic RNA folding mediates assembly of human parechovirus. Nat

427   Commun **8:**5.

17

428   23.   **Boonyakiat Y, Hughes PJ, Ghazi F, Stanway G.** 2001. Arginine-glycine-aspartic acid

429   motif is critical for human parechovirus 1 entry. J Virol **75:**10000-10004.

430   24.   **Seitsonen J, Susi P, Heikkilä O, Sinkovits RS, Laurinmäki P, Hyypiä T, Butcher SJ.**

431   2010. Interaction of alphaVbeta3 and alphaVbeta6 integrins with human parechovirus 1. J

432   Virol **84:**8509-8519.

433   25.   **Al-Sunaidi M, Williams CH, Hughes PJ, Schnurr DP, Stanway G.** 2007. Analysis of a

434   new human parechovirus allows the definition of parechovirus types and the identification

435   of RNA structural domains. J Virol **81:**1013-1021.

436   26.   **Scheres SH.** 2012. RELION: implementation of a Bayesian approach to cryo-EM structure

437   determination. J Struct Biol **180:**519-530.

438   27.   **Karelehto E, van der Sanden S, Geraets JA, Domanska A, van der Linden L,**

439   **Hoogendoorn D, Koen G, van Eijk H, Shakeel S, Beaumont T, de Jong M, Pajkrt D,**

440   **Butcher SJ, Wolthers KC.** 2017. Strain-dependent neutralization reveals antigenic

441   variation of human parechovirus 3. Sci Rep **7:**12075.

442   28.   **Kwakkenbos MJ, Diehl SA, Yasuda E, Bakker AQ, van Geelen CM, Lukens MV, van**

443   **Bleek GM, Widjojoatmodjo MN, Bogers WM, Mei H, Radbruch A, Scheeren FA, Spits**

444   **H, Beaumont T.** 2010. Generation of stable monoclonal antibody-producing B cell receptor-

445   positive human memory B cells by genetic programming. Nat Med **16:**123-128.

446   29.   **Borodavka A, Dykeman EC, Schrimpf W, Lamb DC.** 2017. Protein-mediated RNA

447   folding governs sequence-specific interactions between rotavirus genome segments. Elife **6**.

448   30.   **Borodavka A, Tuma R, Stockley PG.** 2012. Evidence that viral RNAs have evolved for

449   efficient, two-stage packaging. Proc Natl Acad Sci U S A **109:**15769-15774.

450   31.   **Koning RI, Gomez-Blanco J, Akopjana I, Vargas J, Kazaks A, Tars K, Carazo JM,**

451   **Koster AJ.** 2016. Asymmetric cryo-EM reconstruction of phage MS2 reveals genome

452   structure in situ. Nat Commun **7:**12524.

18

453   32.   **Patel N, Wroblewski E, Leonov G, Phillips SEV, Tuma R, Twarock R, Stockley PG.**

454   2017. Rewriting nature's assembly manual for a ssRNA virus. Proc Natl Acad Sci U S A

455   **114:**12255-12260.

456   33.   **Sokoloski KJ, Nease LM, May NA, Gebhart NN, Jones CE, Morrison TE, Hardy RW.**

457   2017. Identification of Interactions between Sindbis Virus Capsid Protein and Cytoplasmic

458   vRNA as Novel Virulence Determinants. PLoS Pathog **13:**e1006473.

459   34.   **Butterfield GL, Lajoie MJ, Gustafson HH, Sellers DL, Nattermann U, Ellis D, Bale JB,**

460   **Ke S, Lenz GH, Yehdego A, Ravichandran R, Pun SH, King NP, Baker D.** 2017.

461   Evolution of a designed protein assembly encapsulating its own RNA genome. Nature

462   **552:**415-420.

463   35.   **Zheng SQ, Palovcak E, Armache JP, Verba KA, Cheng Y, Agard DA.** 2017.

464   MotionCor2: anisotropic correction of beam-induced motion for improved cryo-electron

465   microscopy. Nat Methods **14:**331-332.

466   36.   **Zhang K.** 2016. Gctf: Real-time CTF determination and correction. J Struct Biol **193:**1-12.

467   37.   **Yan X, Sinkovits RS, Baker TS.** 2007. AUTO3DEM--an automated and high throughput

468   program for image reconstruction of icosahedral particles. J Struct Biol **157:**73-82.

469   38.   **Kucukelbir A, Sigworth FJ, Tagare HD.** 2014. Quantifying the local resolution of cryo-

470   EM density maps. Nat Methods **11:**63-65.

471   39.   **Roy A, Kucukural A, Zhang Y.** 2010. I-TASSER: a unified platform for automated protein

472   structure and function prediction. Nat Protoc **5:**725-738.

473   40.   **Schwede T, Kopp J, Guex N, Peitsch MC.** 2003. SWISS-MODEL: An automated protein

474   homology-modeling server. Nucleic Acids Res **31:**3381-3385.

475   41.   **Shakeel S, Westerhuis BM, Ora A, Koen G, Bakker AQ, Claassen Y, Wagner K,**

476   **Beaumont T, Wolthers KC, Butcher SJ.** 2015. Structural basis of human parechovirus

477   neutralization by human monoclonal antibodies. J Virol doi:10.1128/JVI.01429-15.

19

478   42.   **Pettersen EF, Goddard TD, Huang CC, Couch GS, Greenblatt DM, Meng EC, Ferrin**

479   **TE.** 2004. UCSF Chimera--a visualization system for exploratory research and analysis. J

480   Comput Chem **25:**1605-1612.

481   43.   **Emsley P, Lohkamp B, Scott WG, Cowtan K.** 2010. Features and development of Coot.

482   Acta Crystallogr D Biol Crystallogr **66:**486-501.

483   44.   **Humphrey W, Dalke A, Schulten K.** 1996. VMD: visual molecular dynamics. J Mol Graph

484   **14:**33-38, 27-38.

485   45.   **Phillips JC, Braun R, Wang W, Gumbart J, Tajkhorshid E, Villa E, Chipot C, Skeel**

486   **RD, Kale L, Schulten K.** 2005. Scalable molecular dynamics with NAMD. J Comput

487   Chem **26:**1781-1802.

488   46.   **Trabuco LG, Villa E, Mitra K, Frank J, Schulten K.** 2008. Flexible fitting of atomic

489   structures into electron microscopy maps using molecular dynamics. Structure **16:**673-683.

490   47.   **Baker EN, Hubbard RE.** 1984. Hydrogen bonding in globular proteins. Prog Biophys Mol

491   Biol **44:**97-179.

492   48.   **Ippolito JA, Alexander RS, Christianson DW.** 1990. Hydrogen bond stereochemistry in

493   protein structure and function. J Mol Biol **215:**457-471.

494

495   **Table 1: Summary of cryo-EM data collection, refinement, and validation statistics**

496

497   **Figure legends**

498   **Figure 1: Resolution assessment for the HPeV3-Fab complex**

499   (A) **"**Gold standard" FSC curve showing an overall nominal resolution at 2.8 Å.

500   (B) Central cross-section of three-dimensional density map alongside structure colored according to

501   local resolution. Two-, three- and five-fold symmetry axes are labeled by oval, triangle, and penta-

502   gon, respectively.

503   **Figure 2: Visualization of Fab-decorated HPeV3**

504   (A-C) Virus-Fab reconstruction shown radially color-coded (purple 100 Å, yellow 120 Å, light blue

505   140 Å, blue 145 Å, and orange 150 Å).

506   (A) Surface view down a two-fold axis of symmetry. Propeller regions can be seen as a dark blue

507   triangles on the capsid surface, the Fabs are orange.

508   (B) Cutaway view showing RNA (purple) at five-fold vertices inside the viral capsid.

509   (C) Central cross-section with well-defined layers of density corresponding to RNA, capsid, and

510   Fab.

511   (D) Side chains for viral coat proteins VP0 (blue), VP1 (green), and VP3 (light blue), as well as Fab

512   heavy and light chains V_H (orange) and V_L (light brown) respectively.

513   (E) Modeled asymmetric unit with a Fab molecule bound.

514   (F) High resolution at the Fab AT12-015-HPeV3 interface.

515   (G) RNA anchoring on the inner surface of the virus is mediated by a tryptophan (Trp 24) residue

516   from VP3.

517   **Figure 3: Interactions between Fab AT12-015 and HPeV3**

518   (A) Fab binds to an epitope extended across neighboring asymmetric units in the assembled virion.

519   Viral capsid residues that participate in Fab heavy (V_H) and light chain (V_L) binding are highlighted

520   in yellow and are reported in the accompanying table.

521   (B) Stabilizing interactions at the interface. Residues that form hydrogen bonds or a salt bridge are

522   highlighted in yellow on the left, and colored by chain on the enlarged inset on the right. In the in-

523   set, hydrogen bonds are shown as black dashed lines along with a centrally located salt-bridge high-

524   lighted in red.

525   **Figure 4: Antibody AT12-015 blocks virus binding to HT29 cells**

526   (A) Representative fluorescence images of HPeV3 incubated in the presence or absence of varying

527   amounts of AT12-015 antibody. Cell nuclei were visualized using a Hoechst stain (blue) and bound

528   virus was scored by measuring Alexa Fluor 488 intensity (green). Pictures were acquired using a

529   20X objective. Scale bar, 50 µm.

21

530   (B) Effect of preincubation of HPeV3 with different amounts of human monoclonal antibody

531   AT12-015. The results are the average of three repeats of the cold binding assay. The error bars

532   represent the standard error of the mean (SEM).

533   (C) AM28 has no effect on HPeV3 binding to HT29 cells. Representative fluorescence images of

534   HPeV3 incubated in the presence (3μg/ml) or absence (virus no AM28 preincubation) of AM28

535   antibody and added to the cells for binding. Non-infected cells (mock and AM28 no virus) serve as

536   controls. Stained as in (A) and visualized with a 10X objective. Scale bar, 50 μm.

537   **Figure 5: Ordered RNA inside the HPeV3 virion**

538   (A) RNA density segmented from within the virion seen along an icosahedral five-fold axis. The

539   boxed segment of the density is enlarged in B.

540   (B) Eight nucleotides fit to their corresponding density before reaching the helix-coil transition.

541   (C) VP3 tails bridge two adjacent loops of RNA to promote efficient packaging and assembly.

542   Small portion of the capsid VP3 sequence (AAs Leu 16-Arg 26) is shown to clarify the VP3-RNA

543   network on the inner surface of the viral capsid.

544   (D) The binding pocket for RNA on the inside of the capsid involves residues from VP1 and VP3.

545   One RNA loop is stabilized by residues from a single VP1 chain (green) and three VP3 chains (light

546   blue designated by ´, ´´, and ´´´).

547   **Table 1.**

HPeV3-Fab complex	
Data collection	
Voltage (kV)	300
Electron exposure (e-/Å^2 X s)	48
Pixel size (Å)	1.06
Number of micrographs	6,541
Reconstruction	
Number of particles	74,927
B factor (Å^2)	-70
FSC threshold	0.143
Resolution (Å)	2.8
Model building	

22

VP0 (amino acid coverage)	34 - 289
VP1 (amino acid coverage)	25 - 219
VP3 (amino acid coverage)	16 - 256
vRNA (nt)	8
V_H	2 - 119
V_L	2 - 109
Model validation	
MolProbity score	1.55/96th percentile (protein)
Ramachandran outliers (%)	0.93 (protein)
Poor rotamers (%)	3.91 (protein)
Clashscore	0 (protein), 4.35 (vRNA)

548
549

A

Final Resolution = 2.8 Angstrom

rlnFSC_Corrected
rlnFSC_UnmaskedMaps
rlnFSC_MaskedMaps
rlnFSC_PhaseRandomizedMaskedMaps

B

Fab

A B C

D VP0 VP1 VP3 V_H V_L

E V_H VP1 V_L VP3 VP0

F

G VP3 Trp^{24} RNA

A

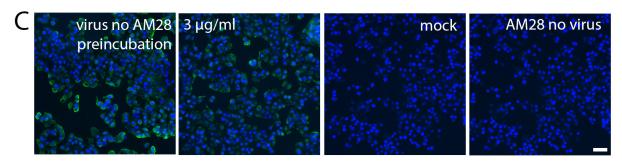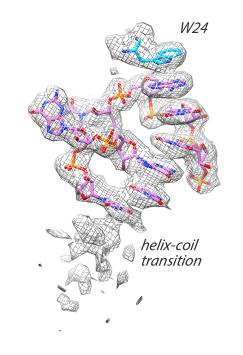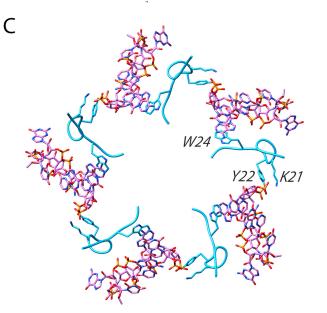|	V_L	V_H
VP0	E285, N289	
VP1	T135, E136, D137, N138	N85, D87, D137, N138, K140, T141, R184
VP1′		P215, T216, G217, S218
VP3′	K99, Y100, V119, T121, T167, D169, H206, G207, H208, Q209	M132, H206, L252, V253

B

A
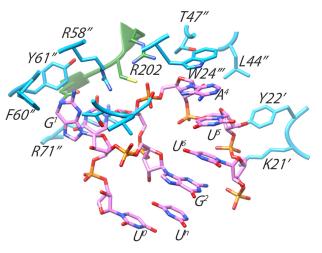
| virus no AT12-015 preincubation | 0.003 μg/ml | 0.03 μg/ml | 0.3 μg/ml |
| 3 μg/ml | 30 μg/ml | mock | AT12-015 no virus |

B

Effect of AT12-015 on virus binding to HT29 cells

1.2

Relative change

1

0.8

0.6

0.4

0.3

0

virus no AT12-015 preincubation | 0.003 μg/ml | 0.03 μg/ml | 0.3 μg/ml | 3 μg/ml | 30 μg/ml | mock | AT12-015 no virus

C

| virus no AM28 preincubation | 3 μg/ml | mock | AM28 no virus |

A

B

W24

helix-coil transition

C

W24

Y22 *K21*

D

T47″

R58″

Y61″ *R202* *W24‴* *L44″*

F60″ *A⁴* *Y22′*

G¹ *U⁵*

R71″ *U⁶* *K21′*

G²

U⁰ *Uⁿ*